Electrodeposition of a novel ternary Fe–W–Zn alloy: Tuning corrosion properties of Fe–W based alloys by Zn addition

Jae-Hyeok Park[1,2], Takeshi Hagio[1,2,z], Yuki Kamimoto[1,2] and Ryoichi Ichino[1,2]

[1]Department of Chemical Systems Engineering, Graduate School of Engineering, Nagoya University, Furo-cho, Chikusa-ku, Nagoya, Aichi 464-8601, Japan.

[2]Institute of Materials Innovation, Institutes of Innovation for Future Society, Nagoya University, Furo-cho, Chikusa-ku, Nagoya, Aichi 464-8601, Japan

[z]Corresponding Author E-mail Address: hagio@mirai.nagoya-u.ac.jp

Abstract

Herein, we report the electrodeposition of a novel ternary Fe–W–Zn alloy. Ternary alloys with compositions of Fe–(29.08–35.96 at.%) W–(1.73–8.16 at.%) Zn were prepared by potentiostatic deposition in citrate–ammonia aqueous solution equipped with an anode chamber. The electrodeposition behavior of the ternary Fe–W–Zn alloys and the effect of the Zn addition were analyzed by cyclic voltammetry and in-situ electrochemical quartz crystal microbalance measurements. Ternary alloys with glossy appearances and smooth surface morphologies were fabricated, with a maximum current efficiency of approximately 43%. Incorporating Zn into the Fe–W alloy structure transformed the alloy structure into an amorphous-like nanocrystalline structure and refined the crystal size to a minimum of 1.45 nm. Potentiodynamic polarization test results showed that the corrosion resistance of the ternary Fe–W–Zn alloy with approximately 2 at.% Zn was distinctly improved compared to the binary Fe–W alloy, both in 1 M H_2SO_4 solution and neutral 3 mass% NaCl solution. Notably, the corrosion resistance was even better than Ni–W alloy in 1 M H_2SO_4 solution, with its unique passivation behavior. The incorporation of Zn was found to be effective for

tuning the corrosion properties of Fe–W alloys.

Introduction

W and its alloys are used in various industrial fields owing to their excellent mechanical, tribological, corrosion resistant, and thermal properties [1–6]. Nevertheless, the fabrication of W alloys is challenging as W has the highest melting point among metals (3422 °C). Electrodeposition is anticipated to be an economical and cost-effective method for preparing W alloy coatings since it only requires temperatures of 20–100 °C. However, the electrodeposition of metallic W from aqueous solution is generally difficult, because it exists as oxyanions in a wide pH range [7,8]. The adsorption of tungstate ions with low hydrogen overvoltage on the cathode surface can cause the current to be consumed by the hydrogen evolution reaction rather than the reduction of W to the metallic state. On the other hand, the induced codeposition of W with iron-group metals such as Fe, Ni, and Co enables W to be reduced to the metallic state [9–11].

Recently, increased attention has been paid to the electrodeposition of binary and ternary alloys comprising W and iron-group metals, such as Fe–W [12–14], Co–W [5,6,15], Ni–W [16–20], and Ni–Fe–W [3,21–26]. These alloys offer advanced properties such as high microhardness, thermal stability, wear resistance, and corrosion resistance. Among them, Ni–W alloys are the most intensively studied. However, the replacement of Ni is increasingly recommended owing to environmental concerns [27]. Moreover, Ni has been reported to trigger skin allergies in humans [28–30]. Therefore, the development of environmentally friendly Fe-based W alloys is of great interest.

One promising application of iron-group metal–W alloy coatings is to replace hard Cr platings made using hazardous hexavalent chromium (Cr^{6+}) [6,13,31,32]. Fe–W alloys have high

thermal stability and high hardness at elevated temperatures. Unlike Cr platings, which gradually decrease in hardness at temperatures above 400 °C [32], the hardness of Fe–W alloys is retained or even increased at high temperatures [33,34]. Considering the thermal operating range of Cr platings, thermal stability is an important property. On the other hand, Fe–W alloys have inferior corrosion resistance to Cr and Ni–W alloy platings [26]. Therefore, the corrosion resistance of Fe–W alloys must be improved before they can be applied as substitutes for Cr plating. To overcome this issue, we propose that Zn could be incorporated into the Fe–W alloy, because Zn-based coatings are widely used to enhance the corrosion resistance of steel. Several studies have reported the electrodeposition of ternary W alloys, such as Ni–W–Cu [35] and Ni–W–P [36], but ternary W alloys with Zn have not yet been investigated. This paper describes our preliminary study on the electrodeposition of ternary Fe–W–Zn alloys. The electrodeposition behavior is discussed based on the effect of the Zn addition to the Fe–W binary system. The corrosion properties of the prepared ternary alloys are evaluated by potentiodynamic polarization tests and compared with those of Ni–W and Fe–W alloys.

Experimental

Application of anode chamber in plating system. The Fe–W plating process uses citrate ions as a metal complexing agent and iron(II) ions. However, the complexing agent decomposes at the anode, and the dissolved oxygen ions oxidize the iron(II) ions to iron(III) [37,38]. This results in insufficient formation of stable metal–citrate complexes, which causes metal hydroxides to precipitate in the alkaline plating bath and deteriorates the stability of the system. In iron and iron alloy plating, chemicals such as ascorbic acid or extra additives are often used to prevent the oxidation of iron(II) ions [39]. However, in this study, the use of

plating additives such as brightener, stress reliever, and grain refiner were avoided to minimize the influence of other chemicals on the electrodeposition of ternary alloys. Instead, an anode chamber was used to prevent potential problems. By separating the plating solution and the anode, decomposition of the organic complexing agent at the anode is prevented, and delays the oxidation of iron(II) ions. A commercial cation exchange membrane (Nafion® NRE-212, DuPont) was used as the ion exchange membrane and H_2SO_4 solution was used as the electrolyte for the anode chamber. Only protons can move from the anode chamber to the plating solution, meaning that the organic complexing agents and metal ions in the plating bath cannot reach the anode.

Preparation of plating baths. Plating baths were prepared by mixing tri-sodium citrate dihydrate (Cit; $Na_3C_6H_5O_7 \cdot 2H_2O$, Nacalai Tesque), ammonium sulfate ($(NH_4)_2SO_4$, Nacalai Tesque), zinc sulfate heptahydrate ($ZnSO_4 \cdot 7H_2O$, Nacalai Tesque), iron sulfate heptahydrate ($FeSO_4 \cdot 7H_2O$, Nacalai Tesque), and sodium tungstate dihydrate ($Na_2WO_4 \cdot 2H_2O$, Nacalai Tesque). Electrodeposition was performed at 80 °C with keeping temperature using a water bath. The total volume of the plating bath was adjusted to 200 mL with distilled water. The pH of the bath was adjusted to 8.0 using sodium hydroxide (NaOH, Nacalai Tesque) and sulfuric acid (H_2SO_4, Nacalai Tesque) solutions. The bath compositions for cyclic voltammetry (CV) measurements are shown in Table 1. The chemical compositions of the plating bath for ternary Fe–W–Zn alloys are given in Table 2. Binary Fe–W alloys were prepared in the same plating bath but without the addition of $ZnSO_4 \cdot 7H_2O$ for comparison of the morphologies and grain size. The prepared baths were purged with Ar gas for 30 min before electrodeposition to remove dissolved oxygen.

CV and electrochemical quartz crystal microbalance (EQCM) measurements. The electrodeposition behavior of the ternary alloys was investigated by CV. The CV measurements were conducted using a potentio/galvanostat (SP-150, Bio-Logic) with a

three-electrode system; a commercial Cu plate (B-60-P05, Yamamoto-MS Co., Ltd) with a surface area of 1 × 1 cm as the cathode, Pt coil as the counter electrode, and Ag/AgCl in saturated KCl solution as the reference electrode. The Cu plate was chemically etched using a concentrated nitric acid solution before use. The CV measurements were performed from the open circuit potential (OCP) to −1.4 V (vs. Ag/AgCl), and then from −1.4 to −0.1 V. The scan rate was 50 $mV \cdot s^{-1}$ in both directions. Electrochemical quartz crystal microbalance (EQCM) measurements were utilized for in-situ characterization of the electrodeposition behavior with linear sweep voltammetry (LSV). Along with the LSV measurements, the frequency change (Δf) caused by the mass change (Δm) of the electrode was measured. The increase in mass due to the precipitation of metal on a quartz crystal causes the resonance frequency to decrease according to Sauerbrey's equation:

$$\Delta f = -C_f \cdot \Delta m \quad (1)$$

where Δf represents the change in resonance frequency, Δm represents the mass change per unit area, and C_f represents the specific constants of oscillator (integer, >0). An Au-coated quartz crystal with a resonance frequency of 10 MHz and area of 0.07 cm^2 was used. The scan rate was 20 $mV \cdot s^{-1}$.

Electrodeposition. A potentio/galvanostat (SP-150, Bio-Logic) was used for electrodeposition process. Commercial steel plate (B-60-P01, Yamamoto-MS Co., Ltd) and Ag/AgCl in saturated KCl solution were used as the cathode and reference electrode, respectively. A Pt coil was used as the anode and placed in the anode chamber filled with 5 wt.% H_2SO_4 solution. Before plating, the steel plate was degreased with ethanol and chemically etched with 10 wt.% H_2SO_4 solution. The deposition area was fixed to 2 × 2 cm by masking the excess area with insulation tape. Constant potential electrolysis (chronoamperometry) was conducted with a potential range of −1.1 to −1.4 V (vs. Ag/AgCl).

A fixed amount of electric charge of 50 C·cm^{-2} was applied with continuous magnetic agitation (stirring) at 500 rpm. The cathodic current efficiency (C_{eff}) was calculated based on the mass gain of the cathode and the elemental compositions of the deposits (determined by energy-dispersive spectroscopy (EDS)) using Faraday's Law of induction:

$$C_{\mathrm{eff}} = \frac{\text{mass of the deposits}}{\text{theoretical mass gain}} \times 100$$

$$= \frac{w \cdot F}{Q} \sum \frac{C_x \cdot N_x}{M_x} \times 100 \qquad (2)$$

where w is the mass of the deposit (g), F is Faraday's constant (96,485 C·mol^{-1}), Q is the passed electric charge (C), C_x (x = Zn, Fe, and W) is the weight fraction of each element in the deposit, N_x is the ionic valence of each element, and M_x is the atomic mass of each element (g·mol^{-3}) [40].

Alloy characterization. The surface morphologies were observed by scanning electron microscopy (SEM, JSM-6330, JEOL). The elemental compositions of the deposits were analyzed by EDS (SEM-EDX Type N, Hitachi). Considering the thinness of the deposited alloy coating, EDS analyses were performed on alloys deposited on Ni plates (NI-313381, Nilaco) to prevent errors associated with the detection of Fe derived from the substrate. X-ray diffraction (XRD; RINT 2500TTR, Rigaku) was conducted with Cu Kα radiation (λ = 0.15456 nm) to verify the crystallinity of the alloys with a scan range of 30° to 90°. The grain sizes of the alloys deposited at each potential were obtained by calculating the parameters derived from the diffraction patterns into Scherrer's equation:

$$D = \frac{k \cdot \lambda}{\beta \cdot \cos\theta} \qquad (3)$$

where D (nm) is the average grain size of the alloy, k is Scherrer's constant (taken as 0.94), λ is wavelength of X-ray sources, β is the full width at half maximum (FWHM), and θ is the peak position.

Corrosion tests. Potentiodynamic polarization tests were performed to evaluate corrosion resistance of the ternary alloys in 1 M H_2SO_4 and 3 mass% NaCl solution at room temperature. The solution was deaerated before use for 30 min with high purity Ar gas to remove dissolved oxygen. The exposed area of the working electrode was fixed to 1 × 1 cm. The corrosion potentials and corrosion current densities of the alloys were calculated using the Tafel equation. The passivation behavior of the alloys was discussed by comparing the results of electrodeposited Ni–19.68 at.% W alloy, Fe–33.10 at.% W alloy, and bare steel plate. The electrodeposition conditions for the Ni–W and Fe–W alloys used for the corrosion test are presented in Table S1. The polarization measurements were performed from −0.4 V (vs. OCP) to +2.5 V (vs. Ag/AgCl) with a scan rate of 1 $mV \cdot s^{-1}$ after stabilizing the OCP.

Results and discussion

CV and EQCM measurement results. Figure 1 presents a series of CV curves for each bath composition. Fig. 1(a) shows how the addition of $(NH_4)_2SO_4$ to the Cit–Zn bath affected the electrodeposition behavior of Zn. At pH values near 8.0, the predominant ionic state of the citrate species was Cit^{3-}, which forms a stable complex with the Zn ions. In the bath without $(NH_4)_2SO_4$, an increase in cathodic current was observed near −1.2 V, which is caused by the electrodeposition of Zn from the Cit–Zn complex; while an increase in anodic current was observed at −1.1 to −0.8 V due to the dissolution of metallic Zn. However, a plateau appeared from −1.25 to −1.4 V, which was possibly caused by the diffusion limitation of the Cit–Zn complex. This plateau almost disappeared by adding 0.8 $mol \cdot dm^{-3}$ of $(NH_4)_2SO_4$ to the Cit–Zn bath, which increased the cathodic and anodic currents during CV. Increased cathodic current indicates the deposition rate of metallic Zn is increased by adding 0.8 $mol \cdot dm^{-3}$ of $(NH_4)_2SO_4$ in Cit-Zn bath. This is supported by EQCM measurement results presented in Fig. S1. The increase in anodic current from -1.2 to -0.8 V also proves that the

amount of electrodeposited metallic Zn was larger in the presence of $(NH_4)_2SO_4$. Considering the bath pH and speciation diagram of ammonium ions (pK_a = 9.26), a small portion existed as NH_3, enabling the formation of Zn–NH_3 complex ions, $[Zn(NH_3)_n]^{2+}$ (n = 1–4). Among these complexes, $[Zn(NH_3)_4]^{2+}$ was anticipated to be the predominant species considering the equilibrium of the Zn–NH_3–H_2O system [41]. Since the stability constant of $[Zn(NH_3)_4]^{2+}$ ($\log \beta$ = 9.34 [42]) is higher than that of the feasible Cit–Zn complex ions, $[Zn(Cit)]^-$ ($\log \beta$ = 5.02) and $[Zn(Cit)_2]^{4-}$ ($\log \beta$ = 6.76) [43], Zn is anticipated to exist mainly as $[Zn(NH_3)_n]^{2+}$. The bath pH of 8.0 is lower than the pK_a of ammonium ions. Hence, metallic Zn can be electrodeposited from $[Zn(NH_3)_4]^{2+}$ [44] as per Equation 4:

$$[Zn(NH_3)_4]^{2+} + 4H^+ + 2e^- \rightarrow Zn + 4NH_4^+ \quad (4)$$

The formation of Zn–NH_3 complex ions therefore enables Zn to be incorporated into the Fe–W alloy by electrodeposition over a wide potential range. The induced codeposition of the Fe–W alloy from the Cit–Fe bath was confirmed by CV, as demonstrated by the curves in Fig. 1(b). The electrodeposition of metallic Fe from Cit–Fe complex ions, $[(Fe)(Cit)]^-$, occurred via the following reaction.

$$[(Fe)(Cit)]^- + 2e^- \rightarrow Fe + Cit^{3-} \quad (5)$$

Therefore, the increase in anodic current at −0.6 V was due to the dissolution of electrodeposited Fe. The addition of 0.05 mol·dm^{-3} of Na_2WO_4 into the Cit–Fe bath drastically increased both the cathodic and anodic currents, implying that induced codeposition of Fe–W alloy took place. Based on the induced codeposition mechanism of Ni–W alloys [7,8] and the speciation diagram for Cit–WO_4^{2-} complexes at pH 8.0 [45], the induced codeposition of Fe–W alloy can occur by the following reactions:

$$[(Fe)(Cit)]^- + [(WO_4)(Cit)(H)]^{4-} \rightarrow [(Fe)(WO_4)(Cit)(H)]^{2-} + Cit^{3-} \quad (6)$$

$$[(Fe)(WO_4)(Cit)(H)]^{2-} + 8e^- + 3H_2O \rightarrow FeW + 7(OH)^- + Cit^{3-} \quad (7)$$

Based on these reactions, $[(Fe)(WO_4)(Cit)(H)]^{2-}$ was considered to be the deposition precursor of the binary Fe–W alloy [11]. In addition, selective cathodic parts of the CV curves (inset in Fig. 1(b)) revealed that the induced codeposition of the Fe–W alloy began near −1.0 V, which is similar to the reduction potential of the Cit–Fe complex. The CV curves of the Cit–W bath did not show an anodic peak, proving that the electrodeposition of metallic W from Cit–WO_4^{2-} complexes (estimated to be $[(WO_4)(Cit)(H)_1]^{4-}$) did not occur. As shown in Fig. 1(c), the addition of 0.01 mol·dm^{-3} of $ZnSO_4$ into the Cit–Fe–W bath shifted the reduction potential and anode current peak position toward the base potential. Moreover, the anodic current decreased, which implies that the induced codeposition of the Fe–W alloy may be partially inhibited by the existence of Zn in the plating bath. Figures 1(d) and (e) show the influence of the Na_2WO_4 content on the electrodeposition behavior of the ternary alloys. The CV curves (see Fig. 1(d)) gradually changed as the amount of Na_2WO_4 added to the Cit–Fe–Zn bath was increased. As the Na_2WO_4 content increased from 0 to 0.05 mol·dm^{-3}, the anode peak potential gradually shifted to a more noble potential, while the anodic current increased significantly when the Na_2WO_4 content reached 0.05 mol·dm^{-3}. In the cathodic regions, the addition of 0.01 mol·dm^{-3} of Na_2WO_4 to the Cit–Fe–Zn bath created a diffusion-controlled range from −1.1 to −1.25 V, as shown in Fig. 1(e). When the Na_2WO_4 content increased to 0.05 mol·dm^{-3}, this diffusion-controlled region disappeared and the cathode current drastically increased. Almost no further change was observed when the Na_2WO_4 content was increased to 0.10 mol·dm^{-3}. This indirectly proves that the aforementioned precursors necessary for the deposition of Fe–W alloys, $[(Fe)(WO_4)(Cit)(H)]^{2-}$, are formed successfully when the amount of Na_2WO_4 exceeds 0.05 mol·dm^{-3}. Two theories on the mechanism of induced codeposition of Fe–W alloy are anticipated from the results. The first is that the electrodeposition of metallic W does not

occur via tungstate ions or Cit–W complex ions, but from precursor complexes such as $[(Fe)(WO_4)(Cit)(H)]^{2-}$. The second is that the ratio of Cit, Fe, and W ions is important for the generation of the precursor complex, thus determining the deposition reaction rate. To confirm the electrodeposition behavior more clearly, EQCM measurements were performed along with LSV. The upper plot of Fig. 2 shows the LSV curves, while the lower plot shows the corresponding frequency variation (Δf) according to the potential scan. In the Cit–Zn bath with 0.8 mol·dm^{-3} of $(NH_4)_2SO_4$, the electrodeposition of Zn from $[Zn(NH_3)_4]^{2+}$ started at about −1.05 V (indicated by the black dashed arrow). However, the deposition amount was relatively low until the potential was almost −1.2 V, and started to increase at potentials below −1.25 V. The electrodeposition of the binary Fe–W alloy in the Cit–Fe–W bath with 0.05 mol·dm^{-3} of Na_2WO_4 started at −1.00 V (indicated by the red dashed/dotted arrow), while the electrodeposition of the ternary Fe–W–Zn alloy in the Cit–Fe–W–Zn bath containing 0.01 mol·dm^{-3} of $ZnSO_4$ started at −1.08 V (indicated by the blue solid arrow), showing that the reduction potential shifts toward the base potential owing to the addition of Zn. This means that the adsorption of $[Zn(NH_3)_4]^{2+}$ to the cathode surface inhibits the induced codeposition of Fe–W alloys. In addition, the difference in frequency variation (Δf) between the binary Fe–W alloy and ternary Fe–W–Zn alloy tended to increase gradually. In conclusion, it is likely that the addition of Zn decreases the current efficiency. Figure 3 shows CV curves measured in Cit–Fe–W–Zn (W: 0.05 mol·dm^{-3}) at various bath temperatures. As the bath temperature was increased, the anodic current gradually increased and the anode peak position shifted to a more noble potential. It has been reported that the induced codeposition of Fe–W alloys occurs more actively with higher tungstate ion concentrations, higher bath temperatures, and higher current densities [12,38]. In the electrodeposition of iron-group metal–W alloys, increasing the bath temperature can lower the overvoltage of the iron-group metals, which may shift the electrodeposition potential to more noble potential.

Reducing the overvoltage can increase the current efficiency of Fe–W alloy electrodeposition and also increase the W content of the coating [46]. Thus, it is likely that Zn will be incorporated into the Fe–W alloy at higher bath temperatures, while lower bath temperatures will induce Zn-based deposits.

Electrodeposition of ternary alloys. The current efficiency and applied current density are shown in Fig. 4 as a function of electrodeposition potential in the range of −1.1 to −1.4 V (vs. Ag/AgCl). The elemental compositions of the Fe–W–Zn alloys are given in Table 3. Increasing the Zn content in the alloy was accompanied by a decrease in the current efficiency. As the electrodeposition potential became more negative, the current efficiency gradually decreased and current density increased. The maximum current efficiency was about 43% at −1.1 V, compared to 15% at −1.4 V. There was a sharp decrease in current efficiency at potentials below −1.15 V. At the same time, in this potential range, the Zn content of the alloys continued to increase as the deposition potential became lower. The EQCM results in Fig. 2 demonstrate that the Zn content of alloys is closely related to the precipitation amount of Zn. Meanwhile, it was confirmed that the W content in the alloys was increased at lower electrodeposition potentials. This is similar to the tendency of increasing W content of iron-group metal–W alloys at higher current densities [19,26]. Various researchers have reported that a lower overpotential promotes the reduction of metallic W and Mo in induced codeposition processes [10,11,47]. The increase in Zn content of the alloy at lower deposition potentials indicates the occurrence of anomalous codeposition, which is normally observed in iron-group metal–Zn alloy plating [48]. The low electrodeposition potential increases the pH at the cathode surface and actively promotes the anomalous codeposition of Zn from $[Zn(NH_3)_4]^{2+}$. This suppresses deposition of the Fe–W alloy, thereby affecting the overall composition of the alloy and the current efficiency of the electrodeposition process [49]. Therefore, in this ternary plating system, it was anticipated that

both the anomalous codeposition of Zn from $[Zn(NH_3)_4]^{2+}$ and induced codeposition of Fe–W alloy take place.

Alloy characterization. SEM images and photographs of ternary alloys fabricated at various electrodeposition potentials are shown in Fig. 5. The obtained ternary alloys were well-adhered to the substrate and exhibited uniform, semi-glossy appearances. There was hardly any evidence of the precipitation of metal hydroxides or adsorption of impurities on the surface, even at low electrodeposition potentials, where excessive hydrogen evolves during the deposition process. Ternary alloys could be obtained over a wide potential range. However, a few cracks were observed at the electrodeposition potential of −1.4 V. Figure 6 compares the surface morphologies and cross-sectional structures of the binary Fe–W alloy and ternary Fe–W–Zn alloy obtained at −1.2 V. The W content of the alloys were similar, but slightly higher for binary Fe–W alloy; however, a significant change in the microstructure was observed in the SEM images of the surface and cross-section. The grain size was found to be drastically reduced by the incorporation of Zn. XRD patterns of the binary and ternary alloys and steel plate are presented in Fig. 7 along with the calculated grain size of the ternary Fe–W–Zn and binary Fe–W alloys. The ternary alloys exhibited similar diffraction patterns to the binary alloy. A single broad peak close to the Fe (110) plane (2θ = 44.74°) appeared near 43.4° in all alloys, indicating that the alloy was lowly crystalline amorphous-like nanocrystalline structure, which corresponds to the results of other reports on Fe–W plating [13,14]. The peak broadening of the diffraction patterns of the ternary alloys indicates that the W and Zn atoms are incorporated into the body-centered cubic (BCC) structure of the Fe lattice [50]. The peaks of the steel substrate were detected in the XRD patterns of alloys deposited at −1.3 and −1.4 V, as the platings were very thin owing to the low current efficiency at these potentials. Figure 7(b) shows that the grain size of the binary Fe–W and ternary Fe–W–Zn alloys decreased proportionally as the electrodeposition

potential become lower. Since a higher current density was applied at lower potentials, it is expected that the grain size decreases as the amount of W and Zn atoms incorporated into the Fe lattice increase. The grain size of the binary Fe–W alloy prepared in this experiment was 1.76–1.88 nm, which is smaller than that found by other researchers (approximately 3.0–4.0 nm) [13]. This low grain size was presumed to be due to the high bath temperature (80 °C) and relatively high W content (29.21–35.34 at.%) in the alloys. The grain size of the ternary alloy was 1.45–1.53 nm, showing that the Zn addition caused grain size refinement. Fig. 8 shows the relation between the grain size and contents of W and Zn of alloys. Increase in Zn content obviously led to crystal refinement while increase in W content in binary Fe-W alloys did not show such enhanced crystal refinement, even at high W content of approximately 35%. This shows the Zn content has a greater influence on the crystal refinement than the W content of the alloy. The surface and cross-sectional images structures shown in Fig. 6 confirm that the alloy microstructure changes owing to the incorporation of Zn into the Fe–W alloy structure.

Anodic polarization measurements. Anodic polarization measurements were conducted for the ternary alloys and comparative materials in deaerated 1 M H_2SO_4 and 3 mass% NaCl solution. The results using 1 M H_2SO_4 solution are shown in Fig. 9. Figure 9(a) shows the polarization curves of the ternary alloys according to the electrodeposition potential. As the electrodeposition potential became lower, the corrosion potential (E_{corr}) of the ternary alloys shifted toward the base potential, and the corrosion current density (I_{corr}) gradually increased. Increasing the Zn and W contents of the alloy shifted E_{corr} to lower values. Since Zn has the lowest potential ($E^0 = -0.76$ V vs. NHE) among the ternary alloying elements, it is possible that E_{corr} reduces as the Zn content increases. However, although W has a higher potential than Fe, it has been reported that increasing the W content in electrodeposited iron-group metal–W alloys can lower the E_{corr} of the deposited alloys [51,52]. This is presumed to be

because an n-type semiconductor is formed by the oxidation of W on the alloy surface to produce WO_3 [53]. The accumulation of negative charge in the WO_3 film has been reported to shift E_{corr} to more negative values [54]. Figure 9(b) shows the polarization curves of the ternary alloys and various comparative materials. The E_{corr} of binary Fe–W alloy (−355.46 mV) was slightly higher than that of the steel plate (−419.81 mV), but similar to that of the Fe–W–Zn alloys fabricated at −1.2 and −1.3 V. The W content of the alloys tended to be related to the electrodeposition potential. The ternary alloy obtained at −1.1 V had an I_{corr} of 21.60 $\mu A \cdot cm^{-2}$, which was the lowest among the ternary alloys and even lower than that of the Ni–W alloy (28.46 $\mu A \cdot cm^{-2}$). The alloy obtained at −1.2 V also had a low I_{corr} value of 31.24 $\mu A \cdot cm^{-2}$. Meanwhile, when the electrodeposition potential became lower than −1.3 V, I_{corr} increased significantly to values much greater than those for the binary Fe–W alloy. Moreover, only the alloys obtained at −1.1 and −1.2 V exhibited two passivation regions with low passive current densities (I_p). The unique first passivation region appeared at −0.15 to +0.41 V, and the second region continued until the potential was greater than +2.5 V. The second passivation region exhibited similar behavior to that of the binary Fe–W alloy containing 33 at.% W. However, the trans-passive potentials (E_t) of the ternary alloys were higher than those of the Fe–W alloy (+2.0 V) and Ni–W alloy (+1.6 V), and continued until the potential reached +2.5 V. This indicates that pitting corrosion in acidic environments will be greatly suppressed. Moreover, the first passivation region is a unique characteristic and is thought to be closely related to the amount of Zn incorporated into the alloy. It is assumed that this passivation behavior was induced by the incorporation of Zn into the crystal lattice of the binary Fe–W alloy. I_p decreased until the Zn content reached around 2 at.% and increased thereafter. Considering that this passivation region disappeared for specimens prepared at −1.3 and −1.4 V, it is likely that incorporating only a particular amount of Zn into the binary alloy has an important role on the overall passivation properties of the alloys;

however, further analysis is necessary to clarify this effect. The anodic polarization curves measured in neutral 3 mass% NaCl solution are plotted in Fig. 10. As shown in Fig. 10(a), the E_{corr} of the ternary alloys decreased as the electrodeposition potential decreased. This result is similar to that in the acidic environment. However, I_{corr} decreased gradually as the potential decreased, which is in contrast with the results of measurements in the acidic environment. The higher contents of Zn and W lowered the I_{corr} of the alloys in neutral NaCl solution. The passivation behavior of the ternary alloy obtained at −1.1 V was similar to that of the binary Fe–W alloy, but the passivation region gradually decreased with the electrodeposition potential. The polarization test parameters and W contents of each alloy are presented in Table 4, and the correlation between the polarization test parameters and Zn content of the alloys is shown in Fig. 11. Figure 11(a) suggests that there is no significant correlation between the Zn content and E_{corr} of the ternary alloys in 1 M H_2SO_4 solution, while Table 4 shows that E_{corr} tended to decrease as the W content increased. The W content of the alloys is therefore likely to be the main factor for determining the E_{corr} in 1 M H_2SO_4 solution. In contrast, in the 3 mass% NaCl solution, the Zn content seemed to have a great influence on the E_{corr} of the ternary alloys. Figure 11(b) shows that the I_{corr} of the binary Fe–W alloy varied significantly when Zn was incorporated into the alloy. A drastic decrease in I_{corr} for ternary alloys in both 1 M H_2SO_4 and 3 mass% NaCl solution was observed when the incorporation of Zn was in the range of 1–2 at.%. This may be attributed to the accelerated formation of the passive layer by the sacrificial dissolution of the small amount of Zn. Further investigation is under way to understand this phenomenon.

Conclusions

In this study, the electrodeposition behavior and corrosion properties of novel ternary Fe–W–Zn alloys were examined and compared. The addition of $(NH_4)_2SO_4$ led to the formation

of stable Zn–NH_3 complex ions, $[Zn(NH_3)_4]^{2+}$, which allowed Zn to be incorporated into the Fe–W alloy over a wide potential range. The electrodeposition behavior of the ternary alloys was determined by the induced codeposition of the Fe–W binary alloy and the independent deposition of Zn from Zn–NH_3 complexes. The calculated current efficiency decreased rapidly as the Zn content of the alloys increased, while EQCM measurements revealed that adsorption of Zn–NH_3 complexes on the cathode surface suppressed the induced codeposition of Fe–W alloy. The incorporation of Zn into the binary Fe–W alloy caused deformation of the alloy structure, resulting in refinement of the crystallite size down to about 1.45 nm. The obtained ternary alloy showed improved corrosion resistance compared to the binary Fe–W alloy, while its corrosion properties were highly dependent on the elemental composition of the alloy. When the Zn content was approximately 2 at.%, the ternary alloys showed improved corrosion resistance in acidic H_2SO_4 solution and in common neutral NaCl solution. This novel plating is a possible candidate for use in a variety of industrial applications, to provide the plated material with properties such as corrosion resistance, hardness, and abrasion resistance.

Acknowledgments

This work was supported by Japan Science and Technology Agency (JST)-OPERA Program, Japan [grant numbers JPMJOP1843].

References

1. O. Younes, L. Zhu, Y. Rosenberg, Y. Shacham-Diamand, and E. Gileadi, *Langmuir.*, **17**, 8270 (2001).

2. O. Younes and E. Gileadi, *Electrochem. solid state Lett.*, **3**, 543 (2000).

3. M. Donten, H. Cesiulis, and Z. Stojek, *Electrochim. Acta.*, **45**, 3389 (2000).

4. N. Tsyntsaru, H. Cesiulis, M. Donten, J. Sort, E. Pellicer and E.J. Podlaha-Murphy, *Surf. Eng. Appl. Electrochem.*, **48**, 491 (2012).

5. D. P. Weston, P. H. Shipway, S. J. Harris, and M. K. Cheng, *Wear.*, **267**, 934 (2009).

6. H. Capel, P. H. Shipway, and S. J. Harris, *Wear.*, **255**, 917 (2003).

7. E. Gileadi and N. Eliaz, *ECS Trans.*, **2**(6), 337 (2007).

8. O. Younes and E. Gileadi, *J. Electrochem. Soc.*, **149**, 100 (2002).

9. E. J. Podlaha and D. Landolt, *J. Electrochem. Soc.*, **143**, 885 (1996).

10. E. J. Podlaha and D. Landolt, *J. Electrochem. Soc.*, **143**, 893 (1996).

11. N. Eliaz and E. Gileadi, *Modern aspects of electrochemistry*, p. 191, Springer, New York (2008).

12. A. Mulone, A. Nicolenco, V. Hoffmann, U. Klement, N. Tsyntsaru and H. Cesiulis, *Electrochim. Acta.*, **261**, 167 (2018).

13. N. Tsyntsaru, J. Bobanova, X. Ye, H. Cesiulis, A. Dikusar, I. Prosycevas and J.-P. Celis, *Surf. Coatings Technol.*, **203**, 3136 (2009).

14. S. Wang, C. Zeng, Y. Ling, J. Wang, and G. Xu, *Surf. Coatings Technol.*, **286**, 36 (2016).

15. V. Vasauskas, J. Padgurskas, R. Rukuiža, H. Cesiulis, J.-P. Celis, D. Milčius and I. Prosyčevas, *Mechanics.*, **72**, 21 (2008).

16. L. Elias and A. C. Hegde, *Surf. Coatings Technol.*, **283**, 61 (2015).

17. M.P.Q. Argañaraz, S.B. Ribotta, M.E. Folquer, L.M. Gassa, G. Benítez, M.E. Vela and R.C. Salvarezza, *Electrochim. Acta.*, **56**, 5898 (2011).

18. R. Juškėnas, I. Valsiūnas, V. Pakštas, and R. Giraitis, *Electrochim. Acta.*, **54**, 2616 (2009).

19. K. A. Kumar, G. P. Kalaignan, and V. S. Muralidharan, *Appl. Surf. Sci.*, **259**, 231 (2012).

20. X. Liu, Z. Xiang, J. Niu, K. Xia, Y. Yang, B. Yan and W. Lu, *Int. J. Electrochem. Sci.*, **10**, 9042 (2015).

21. J. Ahmad, K. Asami, A. Takeuchi, D. V Louzguine, and A. Inoue, *Mater. Trans.*, **44**, 1942 (2003).

22. S.-J. Mun, M. Kim, T.-H. Yim, J.-H. Lee, and T. Kang, *J. Electrochem. Soc.*, **157**, 177 (2010).

23. F. He, J. Yang, T. Lei, and C. Gu, *Appl. Surf. Sci.*, **253**, 7591 (2007).

24. A.L.M. Oliveira, J.D. Costa, M.B. de Sousa, J.J.N. Alves, A.R.N. Campos, R.A.C. Santana and S. Prasad, *J. Alloys Compd.*, **619**, 697 (2015).

25. K. R. Sriraman, S. G. Sundara Raman, and S. K. Seshadri, *Mater. Sci. Technol.*, **22**, 14 (2006).

26. K. R. Sriraman, S. G. S. Raman, and S. K. Seshadri, *Mater. Sci. Eng. A.*, **460**, 39 (2007).

27. N. P. Raval, P. U. Shah, and N. K. Shah, *J. Environ. Manage.*, **179**, 1 (2016).

28. A. Goldenberg, S. Admani, J. L. Pelletier, and S. E. Jacob, *Pediatrics*, **136**, 691 (2015).

29. M. Saito, R. Arakaki, A. Yamada, T. Tsunematsu, Y. Kudo and N. Ishimaru, *Int. J. Mol. Sci.*, **17**, 202 (2016).

30. J. P. Thyssen, *Contact Dermatitis.*, **65**, 1 (2011).

31. N.P. Wasekar, N. Hebalkar, A. Jyothirmayi, B. Lavakumar, M. Ramakrishna and G. Sundararajan, *Corros. Sci.*, **165**, 108409 (2020).

32. P. de Lima-Neto, A.N. Correia, R.A.C. Santana, R.P. Colares, E.B. Barros, P.N.S. Casciano and G.L. Vaz, *Electrochim. Acta.*, **55**, 2078 (2010).

33. A. Mulone, A. Nicolenco, J. Fornell, E. Pellicer, N. Tsyntsaru, H. Cesiulis, J. Sort and U. Klement, *Surf. Coatings Technol.*, **350**, 20 (2018).

34. Y. Ruan, S. Yao, and M. Kowaka, *J. Non. Cryst. Solids.*, **117**, 752 (1990).

35. P. Bacal, M. Donten, and Z. Stojek, *Electrochim. Acta.*, **241**, 449 (2017).

36. H.-h. Zhou, Z.-w. Liao, C.-x. Fang, H.-x. Li, B. Feng, S. Xu, G.-f. Cao and Y.-f. Kuang, *Trans. Nonferrous Met. Soc. China.*, **28**, 88 (2018).

37. M. Izaki, *Modern Electroplating*, p. 461, John Wiley & Sons, Hoboken, NJ (2010).

38. A. Nicolenco, N. Tsyntsaru, and H. Cesiulis, *J. Electrochem. Soc.*, **164**, 590 (2017).

39. D.-Y. Park, B. Y. Yoo, S. Kelcher, and N. V Myung, *Electrochim. Acta.*, **51**, 2523 (2006).

40. X. Qiao, H. Li, W. Zhao, and D. Li, *Electrochim. Acta.*, **89**, 771 (2013).

41. I. Rodriguez-Torres, G. Valentin, and F. Lapicque, *J. Appl. Electrochem.*, **29**, 1035 (1999).

42. L. Patrick and A. William, *Water Chemistry: An Introduction to the Chemistry of Natural and Engineered Aquatic Systems*, p.329, Oxford University Press, New York (2011).

43. S. Capone, A. De Robertis, C. De Stefano, and S. Sammartano, *Talanta.*, **33**, 763 (1986).

44. K. Murase, *Rev. Polarogr.*, **60,** 35 (2014), in Japanese.

45. O. Younes-Metzler, L. Zhu, and E. Gileadi, *Electrochim. Acta.*, **48**, 2551 (2003).

46. M. Zemanová, M. Krivosudská, M. Chovancová, and V. Jorík, *J. Appl. Electrochem.*, **41**, 1077 (2011).

47. M. Ahmadi and M. J. F. Guinel, *J. Alloys Compd.*, **574**, 196 (2013).

48. G. Roventi, R. Fratesi, R. A. Della Guardia, and G. Barucca, *J. Appl. Electrochem.*, **30**, 173 (2000).

49. C. Srivastava, S.K. Ghosh, S. Rajak, A.K. Sahu, R. Tewari, V. Kain and G.K. Dey, *Surf. Coatings Technol.*, **313**, 8 (2017).

50. C. Su, M. Ye, L. Zhon, J. Hou, J. Li and J. Guo, *Surf. Rev. Lett.*, **23**, 1550100 (2016).

51. A. Chianpairot, G. Lothongkum, C. A. Schuh, and Y. Boonyongmaneerat, *Corros. Sci.*, **53**, 1066 (2011).

52. H. Alimadadi, M. Ahmadi, M. Aliofkhazraei, and S. R. Younesi, *Mater. Des.*, **30**, 1356 (2009).

53. M. Anik, *Corros. Sci.*, **48**, 4158 (2006).

54. T. A. Aljohani and B. E. Hayden, *Electrochim. Acta.*, **111**, 930 (2013).

Tables

Table 1. Bath compositions for CV measurements.

Bath type	Concentration ($mol \cdot dm^{-3}$)				
	$Na_3C_6H_5O_7$	$ZnSO_4$	$FeSO_4$	Na_2WO_4	$(NH_4)_2SO_4$
Cit–Zn	0.31	0.01	–	–	0.8
Cit– Fe	0.31	–	0.2	–	0.8
Cit–W	0.31	–	–	0.05	0.8
Cit–Fe–Zn	0.31	0.01	0.2	–	0.8
Cit–Fe–W	0.31	–	0.2	0.05	0.8
Cit–Fe–W–Zn	0.31	0.01	0.2	0.01, 0.05, 0.1	0.8

Table 2. Bath compositions for electrodeposition of ternary Fe–W–Zn alloy.

Bath composition	Concentration ($mol \cdot dm^{-3}$)
$Na_3C_6H_5O_7$	0.26
$ZnSO_4$	0.01
$FeSO_4$	0.2
Na_2WO_4	0.05
$(NH_4)_2SO_4$	0.8

Table 3. Elemental compositions of ternary Fe–W–Zn alloys at various electrodeposition potentials.

Electrodeposition Potential	Composition (at.%)		
	Fe	W	Zn
−1.1 V	69.19	29.08	1.73
−1.2 V	66.17	31.17	2.12
−1.3 V	61.76	34.22	4.03
−1.4 V	55.88	35.96	8.16

Table 4. Potentiodynamic polarization test results of Fe–W–Zn alloys and comparative materials in deaerated 1 M H_2SO_4 and 3 mass% NaCl solution.

Specimen	W content [at.%]	At 1 M H_2SO_4		At 3 mass% NaCl	
		E_{corr} [mV]	I_{corr} [μA/cm^2]	E_{corr} [mV]	I_{corr} [μA/cm^2]
Fe–W–Zn (−1.1 V)	29.08	−288.44	21.60	−502.87	13.91
Fe–W–Zn (−1.2 V)	31.17	−325.19	31.24	−680.11	2.71
Fe–W–Zn (−1.3 V)	34.22	−366.22	726.32	−716.26	5.23
Fe–W–Zn (−1.4 V)	37.12	−377.63	1155.12	−785.87	1.45
Ni–W	19.68	−219.50	28.46	−636.05	1.01
Fe–W	33.10	−353.46	181.17	−491.34	11.27
Fe plate	–	−419.81	179.80	−673.33	1.83

Figures

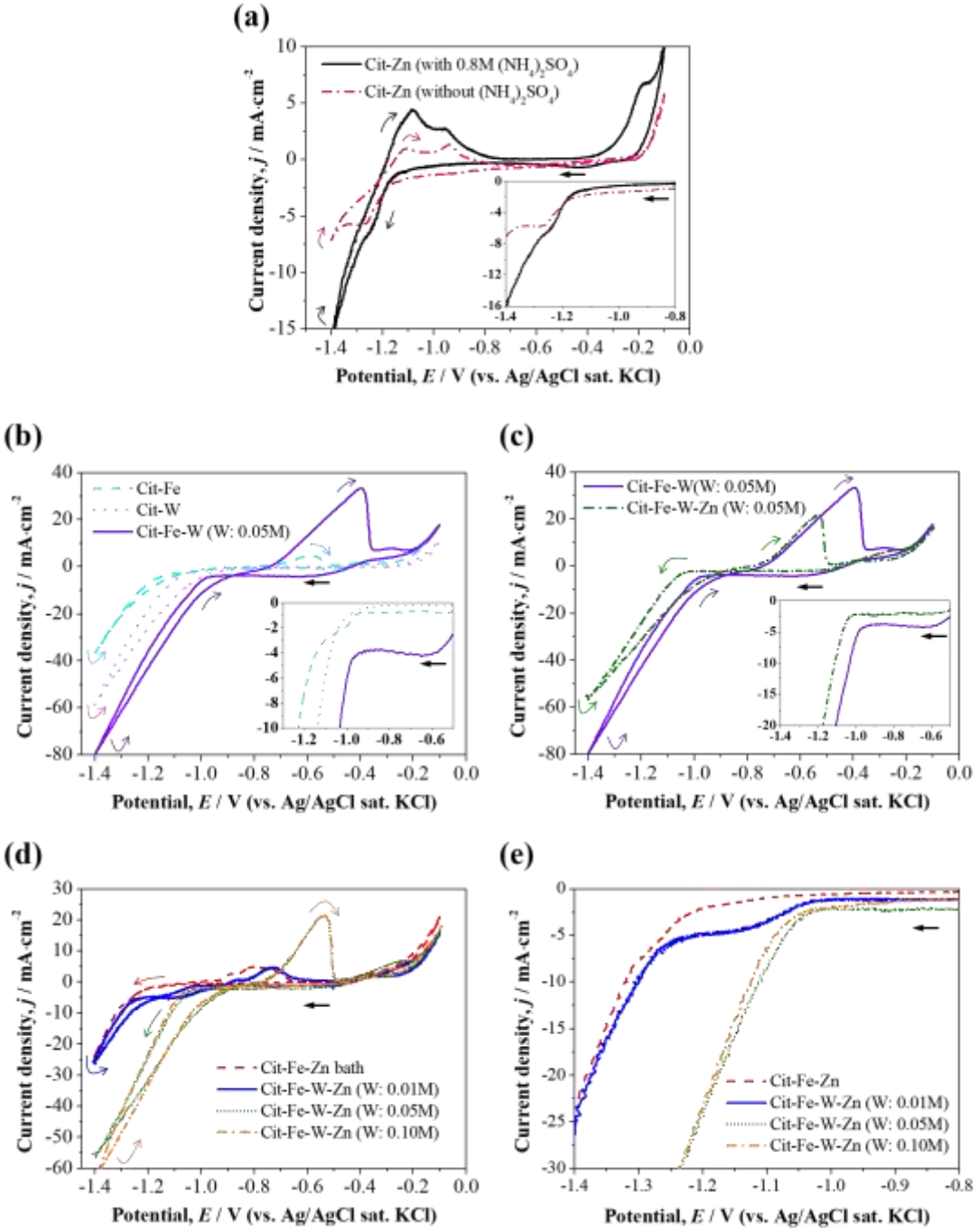

Figure 1.CVs curves in each plating bath: (a) Cit–Zn bath with and without the addition of $(NH_4)_2SO_4$, (b) Cit–Fe, Cit–W, and Cit–Fe–W bath (inside: selective cathodic part), (c) effect of Zn addition on Cit–Fe–W bath (inside: selective cathodic part), (d) influence of Na_2WO_4 contents in Cit–Fe–Zn bath, and (e) selective cathodic parts of (d). The bath

compositions are given in Table 1. The arrows in each plot indicating the scan direction. The scan rate was 50 $mV \cdot s^{-1}$.

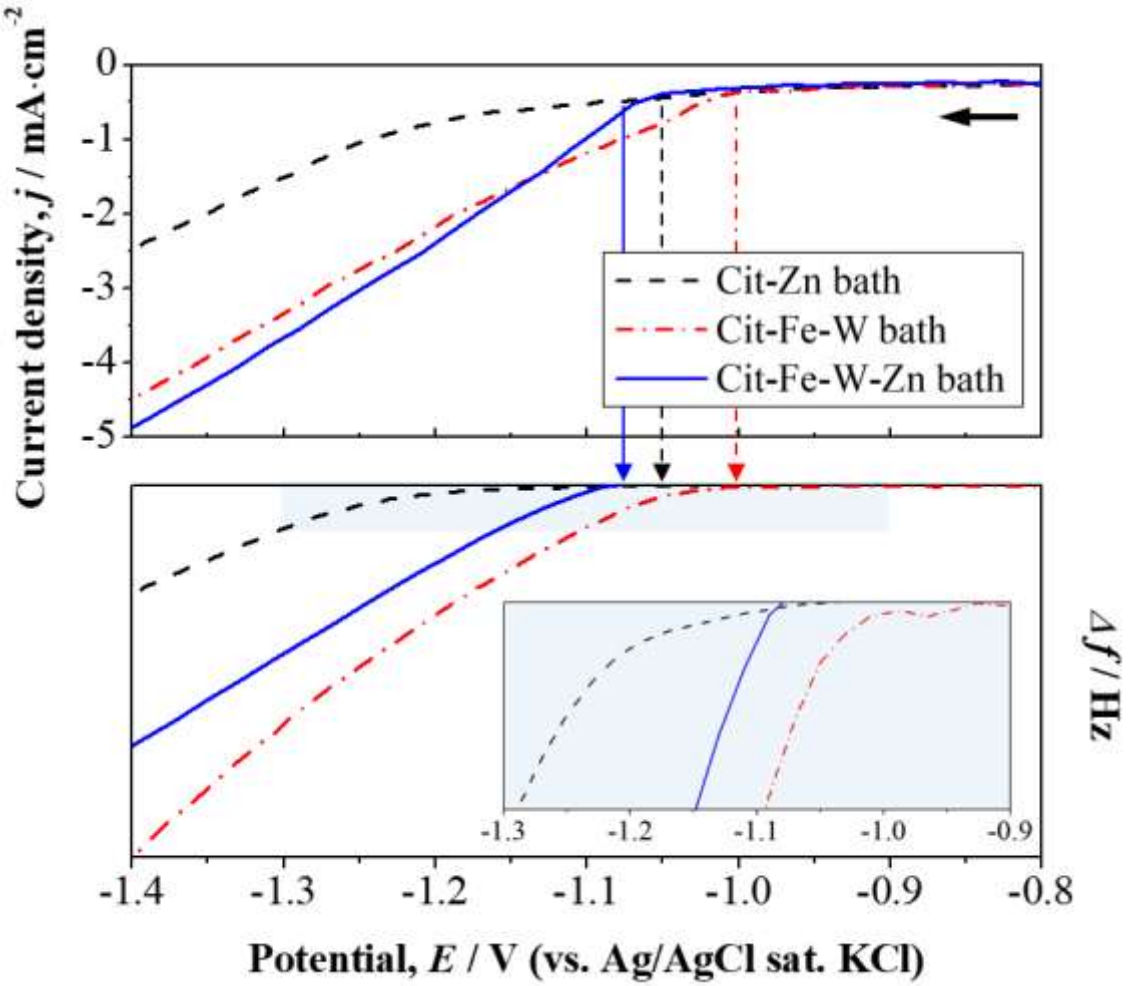

Figure 2. Linear sweep voltammograms (upper plot) and measured frequency variations by EQCM (lower plot). All baths include 0.8 $mol \cdot dm^{-3}$ of $(NH_4)_2SO_4$. Bath composition for each measurement were presented in Table 1. The scan rate was 20 $mV \cdot s^{-1}$.

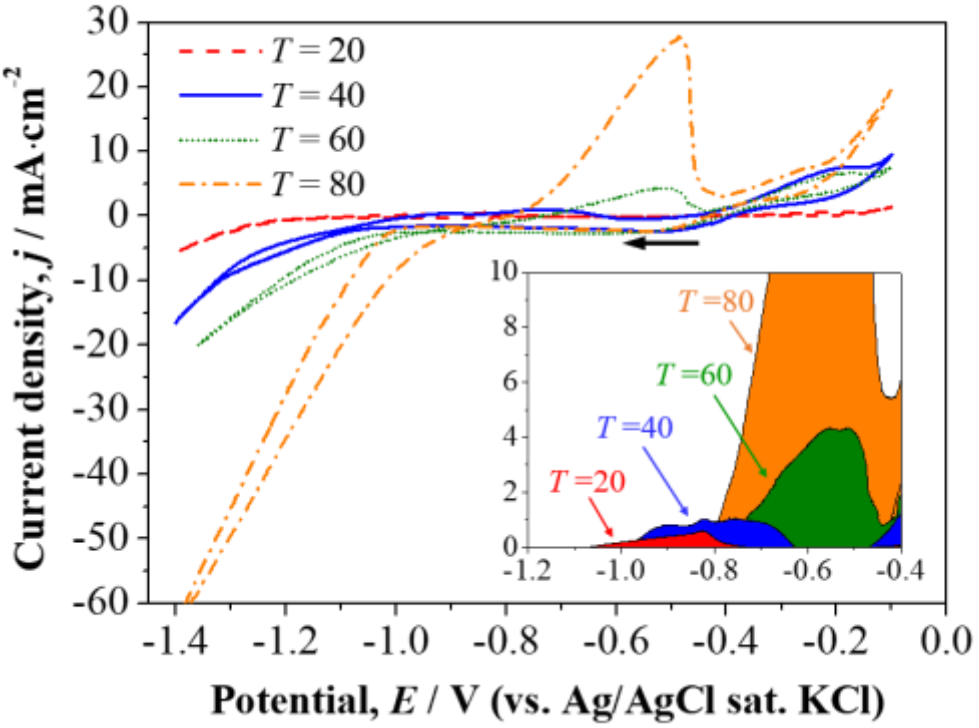

Figure 3. CV curves for Fe–W–Zn bath at various temperatures (bath temperature, T = 20, 40, 60, and 80 °C). Inset: enlarged CV curves between −1.2 and −0.4 V. The colored areas represent the anode current at each bath temperature, the arrow in plot indicates the scan direction.

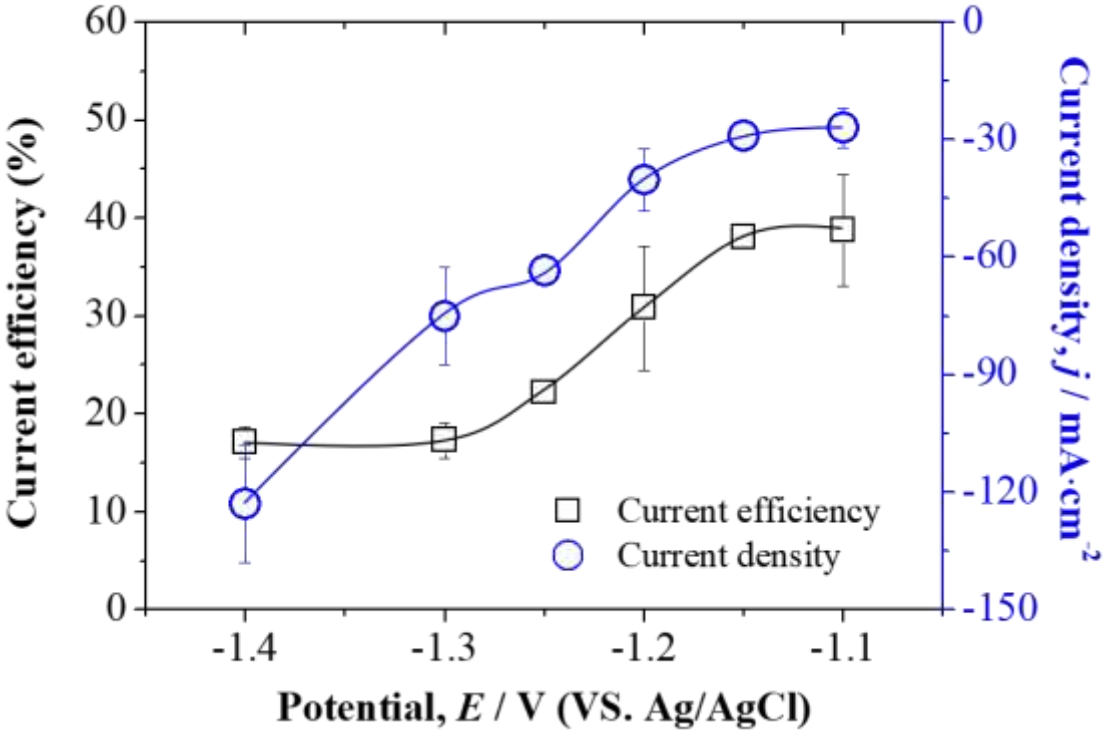

Figure 4. Current efficiencies and applied current densities of ternary Fe–W–Zn alloys as a function of electrodeposition potential. (bath temperature, T = 80 °C)

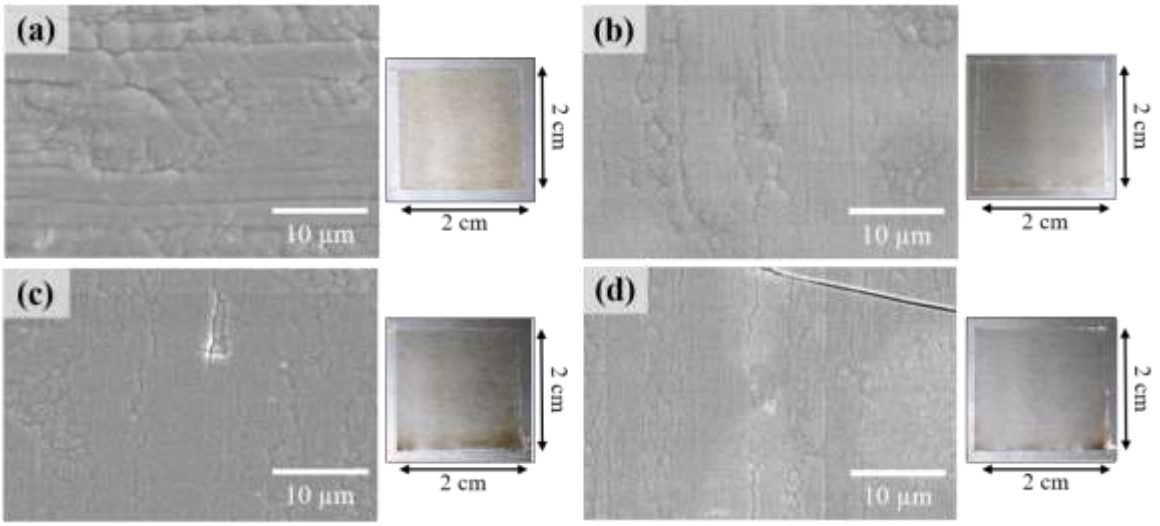

Figure 5. SEM images and photographs of ternary alloys: alloys obtained by electrodeposition potential at (a) −1.1 V, (b) −1.2 V, (c) −1.3 V, and (d) −1.4 V. Equal amount of electric charge Q = 50 C·cm^{-2} was applied for all deposits and the plating area was 2 × 2 cm.

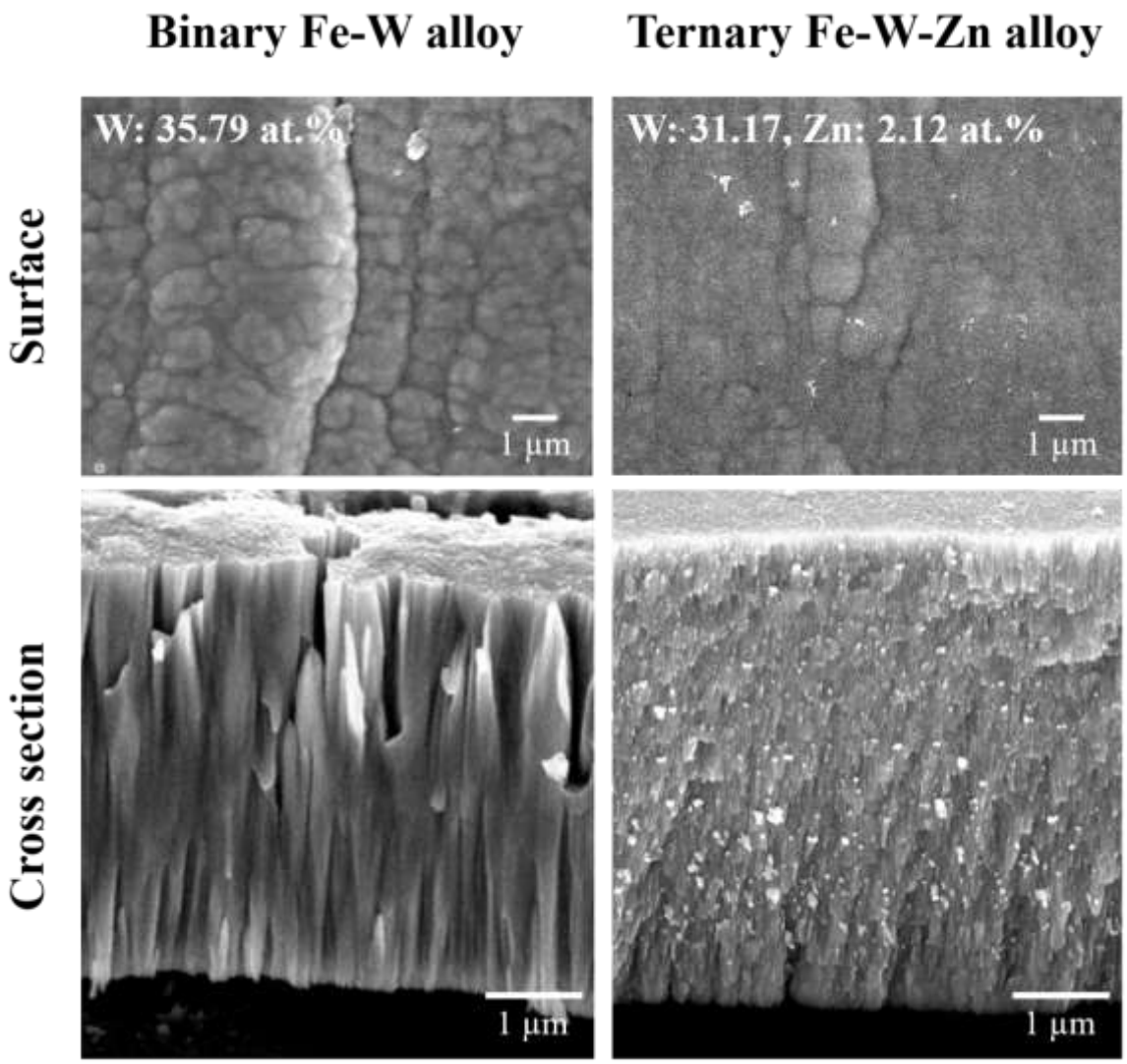

Figure 6. Surface and cross-sectional SEM images for binary Fe–W alloy and ternary Fe–W–Zn alloy. Each alloy was electrodeposited at −1.2 V (vs. Ag/AgCl) and equal amount of electric charge Q = 50 C·cm^{-2} was applied for all deposits. The plating area was 2 × 2 cm.

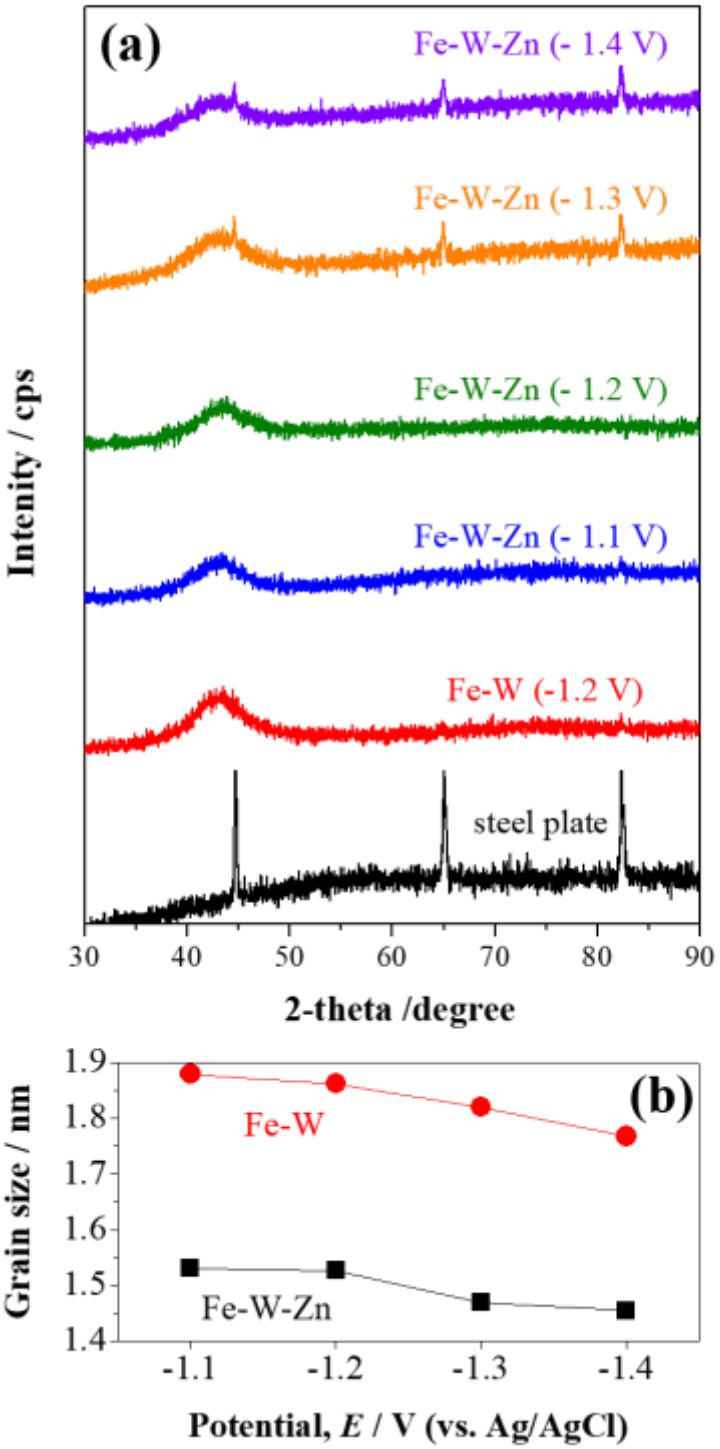

Figure 7. (a) X-ray diffraction patterns for ternary Fe–W–Zn alloys, binary Fe–W alloy, and steel plate and (b) calculated grain size using Scherrer's equation. The intensity (y-axis scale) of each XRD pattern was same as 600 cps.

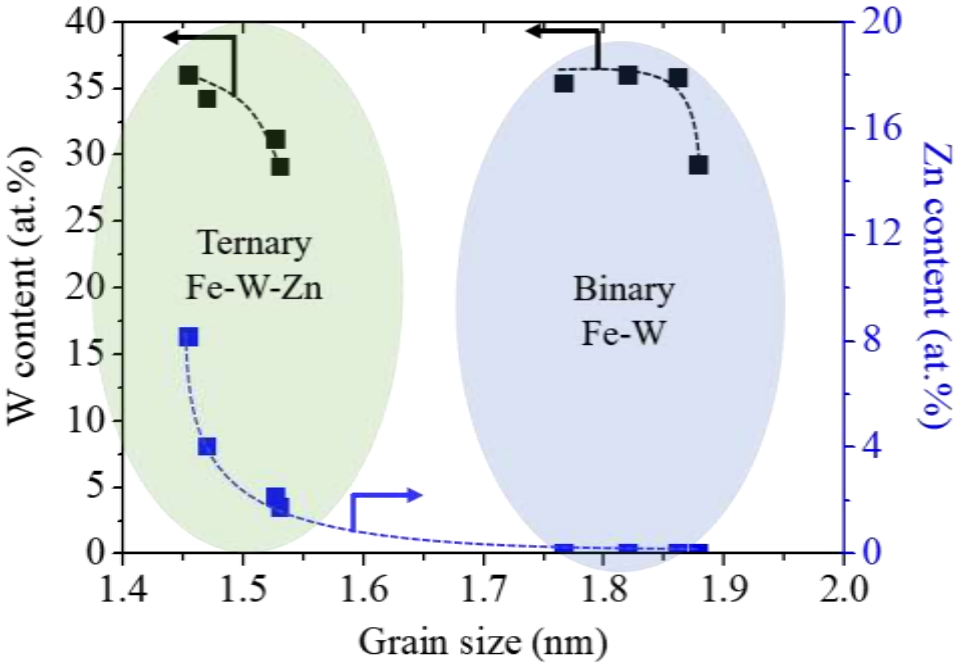

Figure 8. Relation between the grain size and contents of W and Zn of alloys.

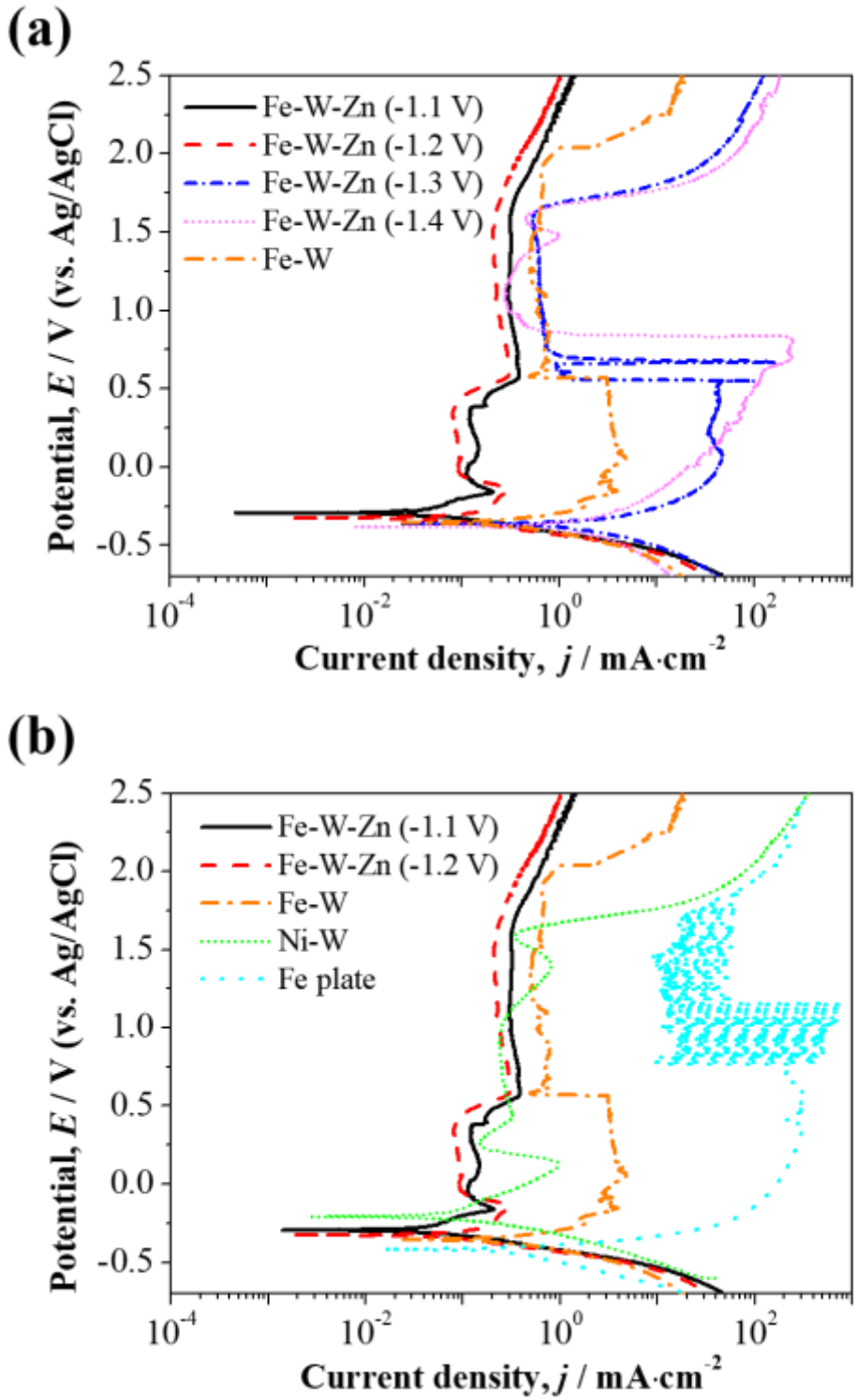

Figure 9. Potentiodynamic polarization curves for (a) ternary alloys and (b) with comparative materials in deaerated 1 M H_2SO_4 solution.

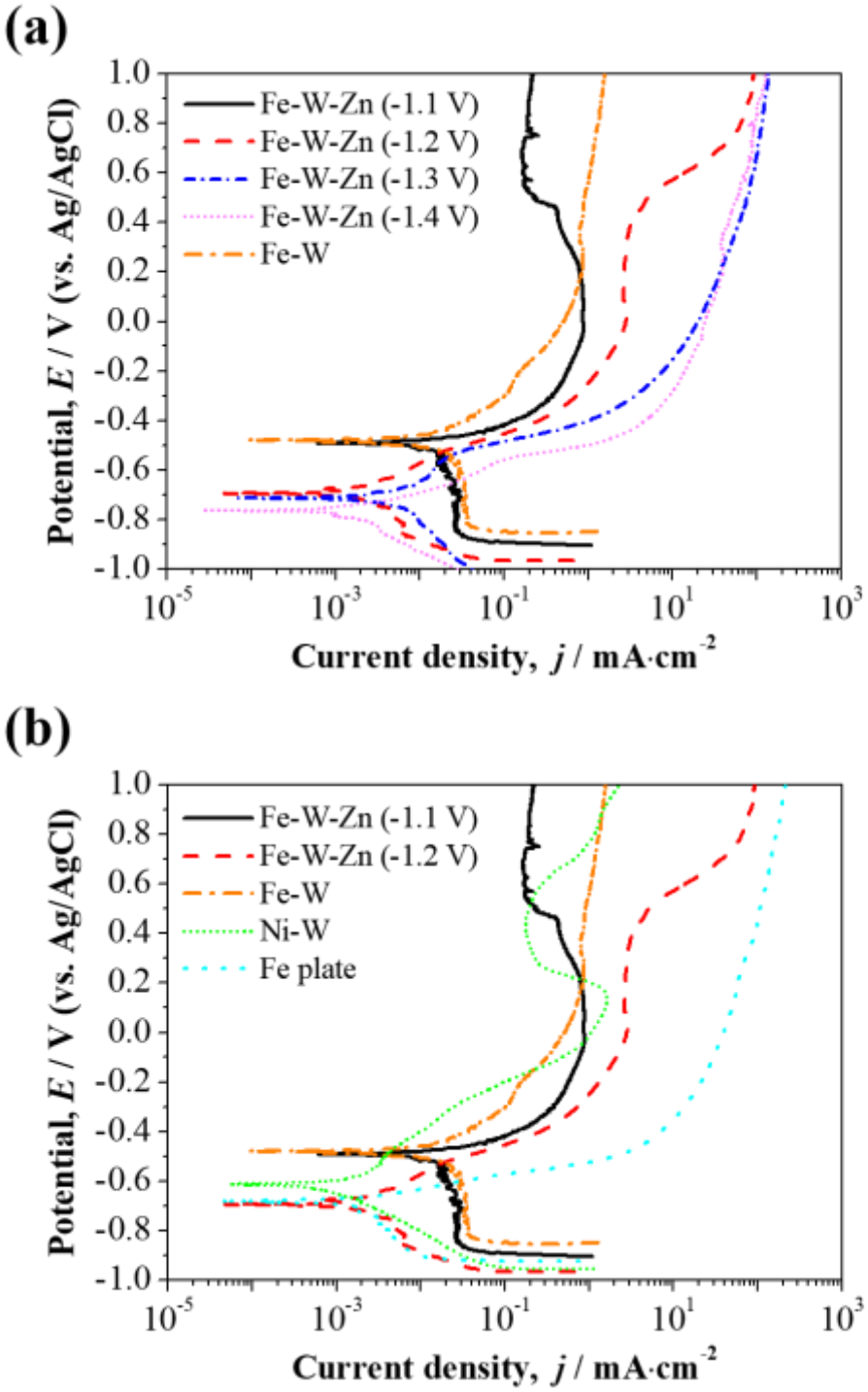

Figure 10. Potentiodynamic polarization curves for (a) ternary alloys and (b) with comparative materials in deaerated 3 mass% NaCl solution.

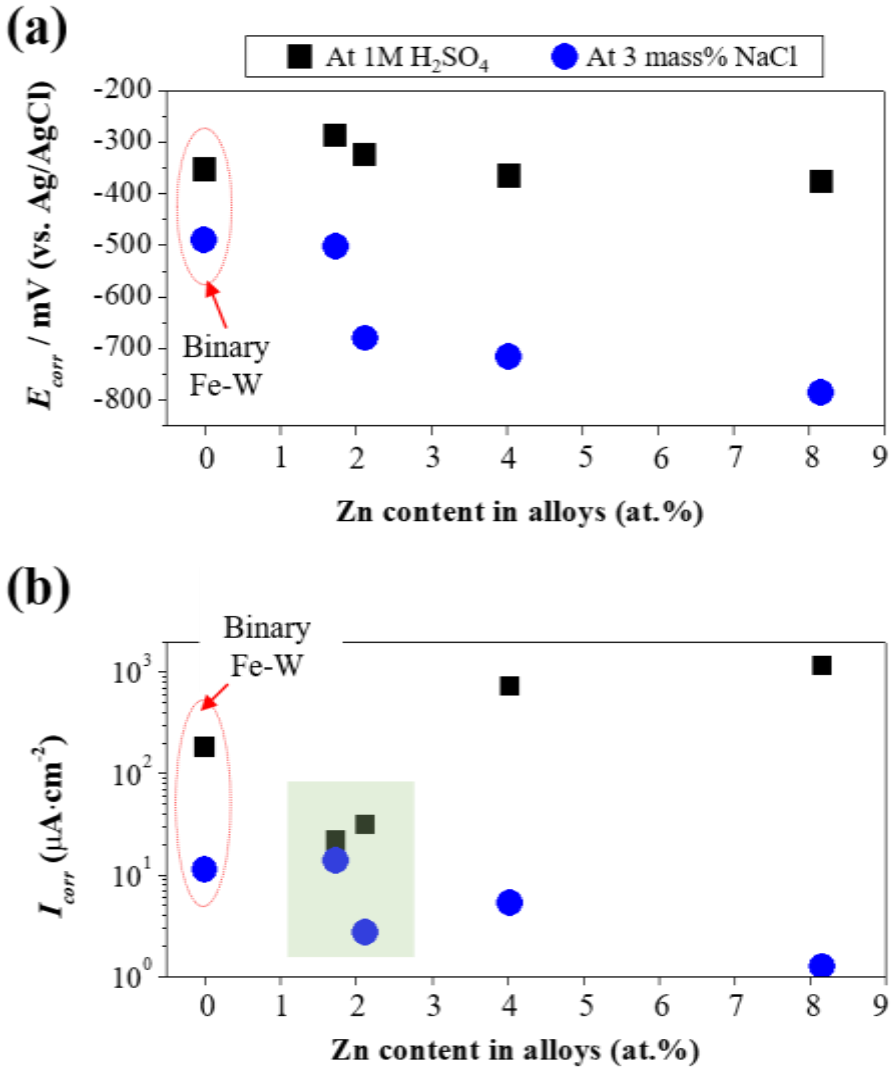

Figure 11. Polarization tests parameters of ternary Fe–W–Zn alloys: (a) Corrosion potential (E_{corr}) and (b) corrosion current density (I_{corr}) as a function of Zn content of alloy.